Efficiency and Stability Enhancement of Fully Ambient Air Processed Perovskite Solar Cells Using TiO$_2$ Paste with Tunable Pore Structure

Seyedeh Mozgan Seyed-Talebi, Iraj Kazeminezhad,* Saeed Shahbazi, and Eric Wei-Guang Diau*

Crystallization and nucleation of the perovskite layer in the mesoscopic perovskite solar cells (PSCs) depend on the nucleation sites of the electron transport layer (ETL). The porosity optimization of TiO$_2$ film as an efficient ETL plays an important role in the performance improvement of PSCs. In the present study, nontoxic carbon spheres synthesized with uniform morphology and controllable size under hydrothermal conditions and used as a template to generate the tunable porous TiO$_2$ films. Furthermore, the effect of porosity modification of TiO$_2$ on the formation of perovskite films with large grain size is studied in an ambient atmosphere with humidity higher than 50%. The best TiO$_2$ film is produced with carbon spheres 8 wt% (C8), which results in the formation of a pinhole-free, and compact-packed perovskite layer. The fully air processed PSC device with the ETL made of C8 film exhibits an efficiency of 16.66% with reduced hysteresis, which is much superior in performance compared to the standard cell (11.72%). It is believed that this porosity optimization of TiO$_2$ layer is a simple practical strategy for improved stability of fully air processed efficient perovskite solar cells and usable for the fabrication of reproducible compact perovskite layers in uncontrolled laboratories.

1. Introduction

In the past few years, perovskite solar cell (PSC) became an interesting subject to study due to recent rapid progress on its device performance. In spite of achieving an impressive power conversion efficiency (PCE) of 25.2% for single junction perovskite based solar cells and certifying by the National Renewable Energy Laboratory,[1] developing an air-processed high-efficiency PSC is still challenging for future commercialization.[2–6] The fabrication process for high-efficiency PSCs needs to perform under highly controlled atmospheric conditions in the N$_2$-filled glove boxes with only trace levels of oxygen and water.[7] Therefore, the deposition in a vacuum environment under controlled atmospheric conditions, will greatly increase the preparing cost and not suitable for large-scale manufacturing. One of the key factors towards large-scale high-efficiency PSCs is controlling the growth conditions of the perovskite layer using interface engineering between perovskite absorber and mp-TiO$_2$.[8–11] In recent decades, carbon-based materials have been widely explored as important materials in both theoretical and experimental types of research.[12–15] The utilization of carbonaceous materials as ETL in the solar cells has improved interface defect passivation, resistances and UV stability of perovskite solar cells.[16,17]

The crystallization of an excellent perovskite layer with full surface coverage and no defects in its grain structure is affected greatly by an enhancement in nucleation at mesostructured interfacial sites.[18] High pore-filling of the mp-TiO$_2$ layer prevents perovskite crystals from decomposition into PbI$_2$. Recent researches demonstrated that tuning the porosity of TiO$_2$ film was effective for PSCs to achieve high performances.[19–22] Increasing the porosity of TiO$_2$ layer can promote an easy and complete infiltration of perovskite into the TiO$_2$ layer. Many research groups have been reported different methods of controlling the mesoporous networks of mp-TiO$_2$.[20–28] The facile method of controlling the porosity of mp-TiO$_2$ by the carbon sphere as a template for fabrication of porous TiO$_2$ hollow sphere and nanoparticle-based photoanodes is used

Dr. S. M. Seyed-Talebi, Prof. I. Kazeminezhad
Department of Physics
Faculty of Science
Shahid Chamran University of Ahvaz
Ahvaz 61357-43135, Iran
E-mail: i.kazeminezhad@scu.ac.ir
Dr. S. M. Seyed-Talebi, Dr. S. Shahbazi, Prof. E. W.-G. Diau
Department of Applied Chemistry and Institute of Molecular Science
National Chiao Tung University
1001 Ta-Hsueh Rd., Hsinchu 30010, Taiwan
E-mail: diau@mail.nctu.edu.tw
Prof. I. Kazeminezhad
Center for Research on Laser and Plasma
Shahid Chamran University of Ahvaz
Ahvaz 30010, Iran
Prof. E. W.-G. Diau
Center for Emergent Functional Matter Science
National Chiao Tung University
1001 Ta-Hsueh Rd., Hsinchu 30010, Taiwan

in dye-sensitized solar cells (DSSC) for light scattering and improving dye absorption.[29–31] Although dye and perovskite based solar cells can borrow some technologies from each other, we cannot exactly judge this facile method of controlling the mp-TiO$_2$ porosity by carbon sphere templates can be an effective strategy for the efficiency improvement of fully ambient processed PSCs. However, to our knowledge, there has been no report on the use of carbon sphere templates to change the mesoporous networks of mp-TiO$_2$ film in PSC and its effect on the formation of a pinhole-free perovskite layer and its stability which is important for commercial applications.

In this study, we present the effect of porosity modification of TiO$_2$ layer on the fully ambient processed formation of compact perovskite films in detail, and found that a higher infiltration of perovskite in mp-TiO$_2$ film results in forming high-quality perovskite films with large grain size and smooth surface, which can effectively suppress charge recombination in the interface by decreasing the contact barrier between the TiO$_2$/CH$_3$NH$_3$PbI$_3$ interfaces, and improve the transport of carriers in the PSCs.

Here, we fabricated the CH$_3$NH$_3$PbI$_3$ layer using the atmospheric pressure vapor-assisted solution processing (AP-VASP) method by exposing the PbI$_2$ film to CH$_3$NH$_3$I vapor in the oven (**Figure 1**a). Using this technique under fully ambient air processed conditions can largely improve the coverage of a compact perovskite layer with uniform grain structure up to micrometers on the surface of ETL.[32–34] Although the best optimal power conversion efficiency of 13.5%, was achieved using AP-VASP method for the CH$_3$NH$_3$PbI$_3$-based perovskite solar cells in the world, a higher degree of reproducibility and easily generating of an interconnected perovskite crystals size can attain under the air processing condition of humidity ambient atmosphere more than 50%.
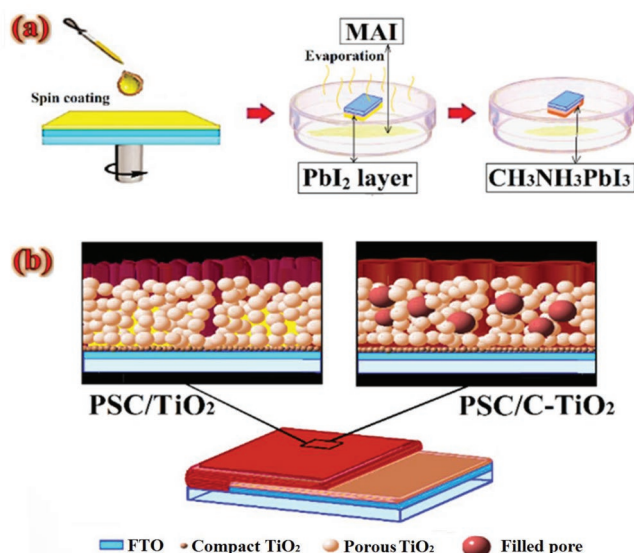
The combination effect of PbI$_2$ and MAI in the crystallization and morphology of mesoscopic CH$_3$NH$_3$PbI$_3$ based PSCs discussed in previous reports.[35–40] In the conventional solution processes, the porous structure of TiO$_2$ hindered the diffusion of CH$_3$NH$_3$I into the pore channel of TiO$_2$ filled by PbI$_2$, resulting in relatively small amounts of unreacted PbI$_2$ remaining in the finally obtained perovskite solar cell.[41–43] Therefore, the crystallization process maybe results in some large crystals on the TiO$_2$ surface but poor coverage due to the localized nucleation of the perovskite layer which tends to obstruct the continual diffusion of MAI to react with PbI$_2$.[44,45]

The fast combination of PbI$_2$ and MAI at the outside capping layer, leading to a small contact area between perovskite and TiO$_2$ layer. In addition, it seems most of PbI$_2$ is converted to the perovskite, but some amounts of unreacted PbI$_2$ maybe remained in the interface of the TiO$_2$/perovskite layer. The residual PbI$_2$ has a detrimental effect on carrier separation and blocks the transformation of electrons from CH$_3$NH$_3$PbI$_3$ to TiO$_2$ inducing a decrease in PCE of PSCs.[46–48] In comparison with solution methods, in the VASP methods, the over-rapid intercalating reaction rate between PbI$_2$ and MAI can reduce.[49–51] Therefore, under the slow MAI evaporation, more nuclei are generated on the substrate and grains will continuously grow in a depressed rate by forming an extremely uniform and flat film with no pinhole and uncovered area on the surface.

In the present work, by porosity optimization of TiO$_2$ layer, more easy mass migration caused more MAI diffusion in PbI$_2$ lattice and excellent pore filling. While a standard ETL is used, irregular size of grains is still observed (see Figure 1b), suggesting insufficient nucleation before crystallization of the perovskite layer. The porosity modification process assisted by the MAI flow during the AP-VASP approach promotes a large number of nuclei before crystallization results in a pinhole free, denser, and flat perovskite film formation without the presence of PbI$_2$ impurities. The growth of the perovskite deep inside the PbI$_2$ layer to reach and contact with TiO$_2$ results in obtaining a pure perovskite layer with larger crystals and more electron injection.[46,48]

2. Results and Discussion

In this section, the characterization of carbon spheres and modified TiO$_2$ pastes by carbon paste will be firstly explained. The effects of the carbon sphere template removal on the pore morphology were then investigated. In the end, the modified mp-TiO$_2$ paste was used to build perovskite solar cells according to the procedure described in the experimental section (Supporting Information).

2.1. Characterizations of Carbon Spheres

Morphology and narrow size distribution of synthesized carbon spheres were investigated by transmission electron microscopy (TEM) and field emission scanning electron microscopy (FESEM) observations. **Figure 2** demonstrates typical TEM and FESEM images of obtained carbon spheres. Synthesized carbon spheres have a regular and perfect shape with an average diameter of about 85 ± 5 nm.
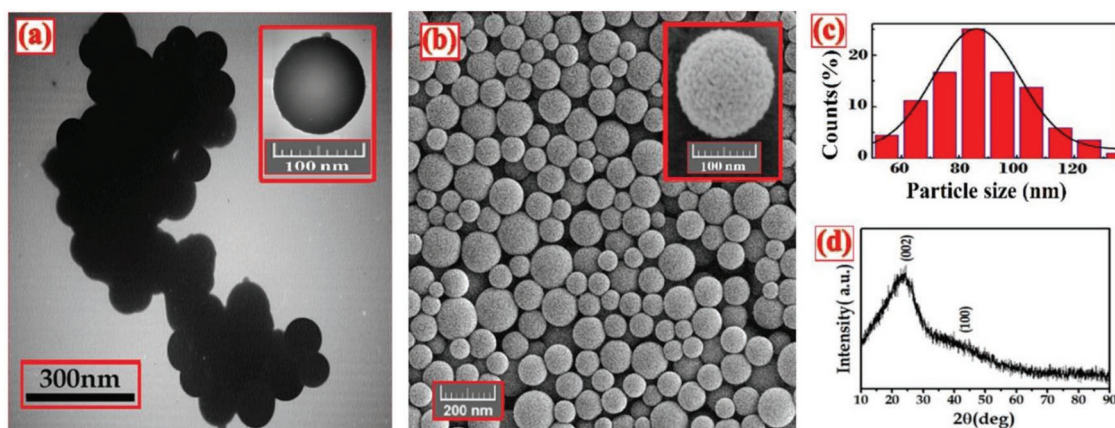

Figure 1. a) Preparation process for depositing CH$_3$NH$_3$PbI$_3$ layer by AP-VASP method, and b) Schematic illustration of perovskite growth on pure and modified TiO$_2$ layer; Size of particles and thickness of layers are not in scale.

Figure 2. a) TEM, b) FESEM, c) particle size distribution, and d) XRD pattern of amorphous carbon nanospheres.

From the X-ray diffraction (XRD) result, we found that carbon spheres with graphite like structure show the wide diffraction patterns around $2\theta \approx 23°$ and $\approx 43.1°$, which can be indexed as preferred (002) and (100) orientation of graphitic planes,[52–54] respectively.

The experimental analysis of elemental mapping (MAP) pattern, energy dispersive X-ray spectroscopy (EDX), and thermogravimetric analysis (TGA) of the samples are shown in **Figure 3**. It can be seen that carbon spheres are composed of carbon and oxygen which amount of carbon is higher than that of oxygen (Figure 3a,b). Oxygen peak can be appeared due to incomplete decomposition of sucrose, adsorption of water on the surface of carbon spheres. It is apparent from the TGA curve (Figure 3c), in a one-step between 35 and 700 °C, all of the carbon templates burned out. An initial decrease of 6 wt% in the weight may be related to the moisture content of carbon spheres.

2.2. Modification of TiO₂ Layer with Different Porosity

All pastes were synthesized according to those reported elsewhere;[55] the preparation details can be found in the Supporting Information. The morphology and composition of the mp-TiO₂ pastes using the carbon sphere in different contents are shown as FESEM images in **Figure 4**. The average diameter of TiO₂ nanoparticles is in the range of 15–20 nm for all prepared pastes.

To clarify the relationship between pore size distribution and rate of doped carbon, the average size percentages of resultant pores in the different mp-TiO₂ layers were calculated using digimizer software from FESEM image of Figure 4 and demonstrated in **Figure 5**. As one can see, by increasing the weight ratios of carbonaceous templates in the pastes, larger pores in those films were observed. Although the average size of the
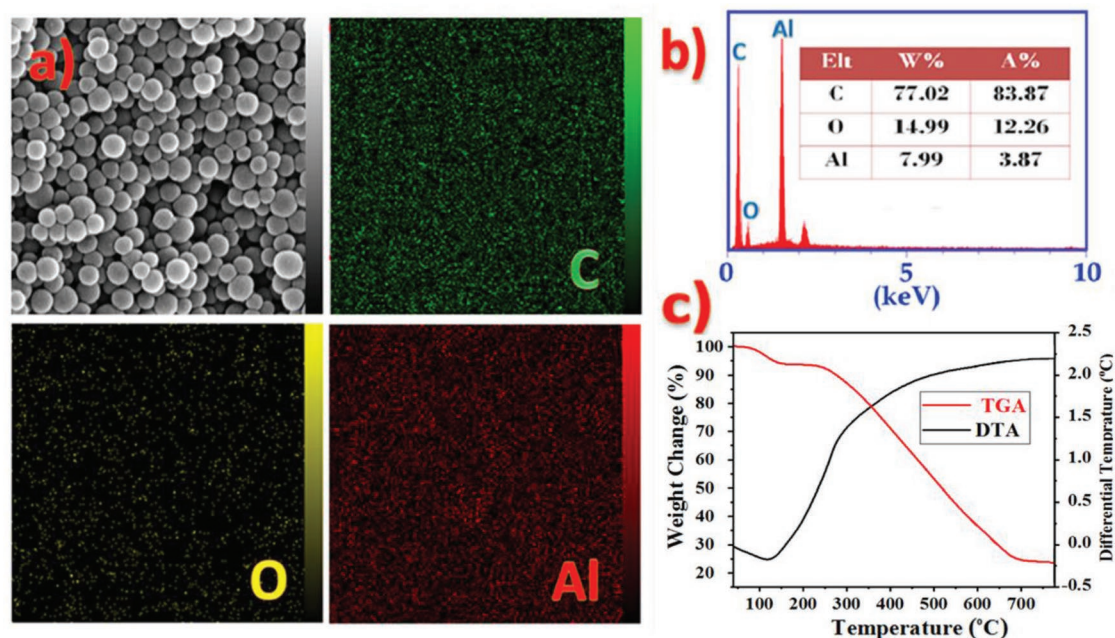

Figure 3. a) MAP pattern, and b) Corresponding EDX spectrum of carbon spheres on top of the Aluminum substrate. The peak of Al comes from the Aluminum substrate used in the measurements. c) Thermo gravimetric analysis (TGA) of prepared carbon spheres.
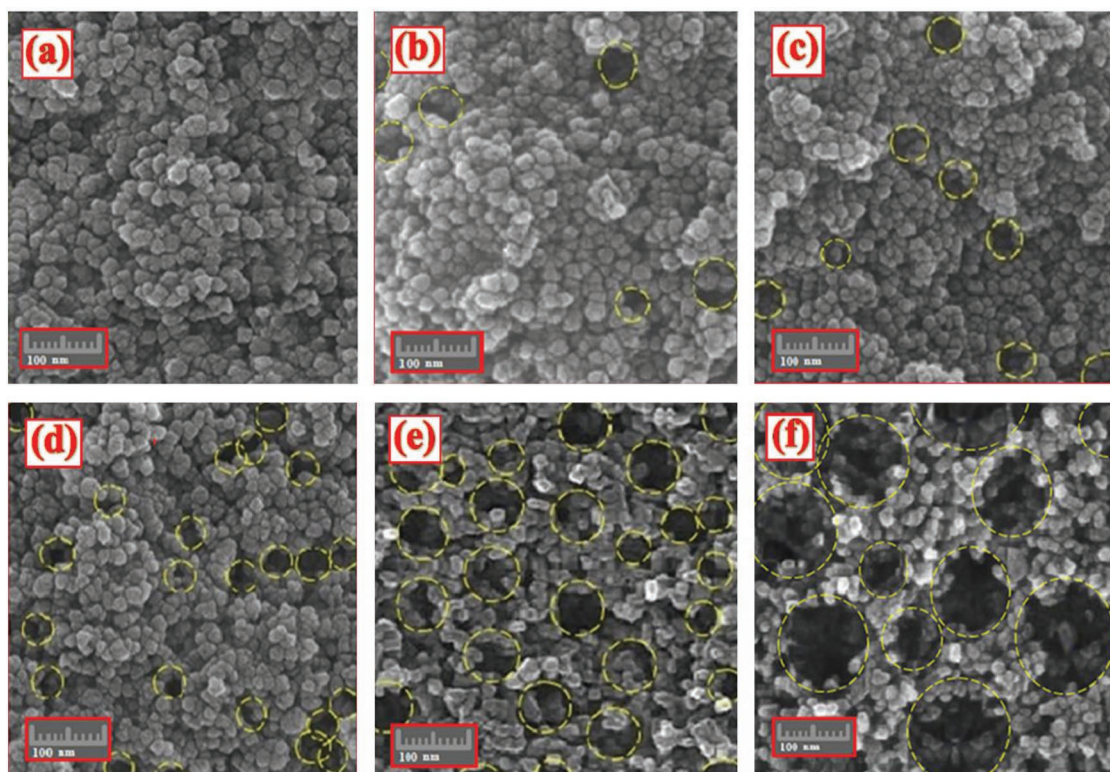
Figure 4. The FESEM images at a very low magnification of the surfaces of modified TiO$_2$ pastes obtained from a) 0 wt%, b) 2 wt%, c) 4 wt%, d) 8 wt%, e) 10 wt%, and f) 20 wt% of carbon spheres after sintering at 450 °C for 30 min.

TiO$_2$ nanoparticles in all pastes was in the same range, the overall sizes and shapes of pores were random.

It can be seen that the pastes made of 8 wt% (C8) carbon spheres exhibit better porosity distribution with greater

Figure 5. Pore size distribution of modified TiO$_2$ pastes obtained by Digimizer from FESEM images of a) C2, b) C4, c) C8, d) C10, and e) C20 after sintering at 450 °C for 30 min.

homogeneity and smooth surfaces compared to other porous TiO$_2$ pastes. When the carbon content is more than 10 wt%, the larger pores appeared (≈136 nm) and their relative percentage increases with adding more carbon spheres. Therefore, the resultant TiO$_2$ layers are not mesoporous and some trap exhibited especially in the grain boundaries of fabricated perovskite layers.

When very large voids were produced, the TiO$_2$ layer tends to crack which could increase the unfavored electron–hole recombination because of the contact between the conductive glass and the perovskite layer.

The above results demonstrated that the preparation of a good porous TiO$_2$ thin film after sintering is highly relative to the enhancement of sufficient carbon spheres to the TiO$_2$ paste. The pores with uniform size distribution in the C-TiO$_2$ paste (content carbon spheres) as effective light scattering centers extend the light traveling distance, thereby improve the optical absorption of the ETL. The pores in the scale of tens of nanometers shown in the cross-section image revealed in Figure S1 in the Supporting Information, also confirm the highly porous property of optimized TiO$_2$ paste (C-TiO$_2$), which is beneficial for the fully pore-filling of perovskite. Due to reducing the cell performance of devices made of less homogeneous TiO$_2$ films with very rough surfaces, more increase in carbon contents (>8 wt%) did not exhibit any further improvement effects.

The Fourier transform infrared (FT-IR) spectrum of a typical C-TiO$_2$ paste without sintering was similar to that recorded for pure paste (Figure S1c, Supporting Information). An increase
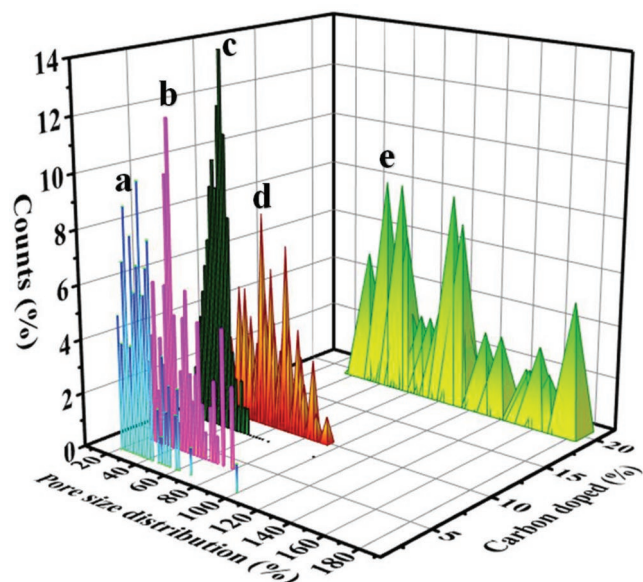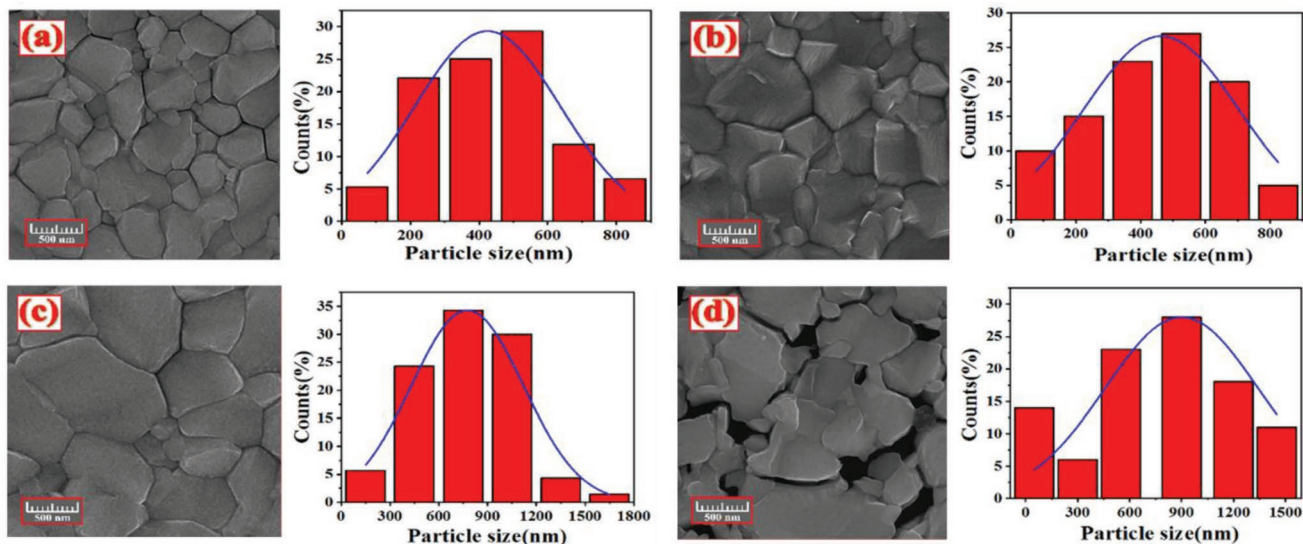
Figure 6. The FESEM images of deposited perovskite layer on the surfaces of modified TiO_2 pastes obtained from a) 0 wt%, b) 4 wt%, c) 8 wt%, and d) 10 wt% of carbon spheres content.

in the different peak intensities is assigned as mixing of carbon spheres on the TiO_2 surface.

The TGA curves of pure and modified TiO_2 paste were characterized by a continuous weight loss of materials from room temperature to near 700 °C. The TGA curve of TiO_2 paste showed an initial large step weight loss ($\Delta m = 64.66\%$) between 35 and 210 °C which was considered due to the elimination of water and α-terpineol (can be removed at 125 °C) as a solvent. First stage weight loss value for C-TiO_2 paste in the TGA curve is also attributed to the burning of carbon spheres. As the carbon spheres amount was increased in C-TiO_2 paste the amounts of surface adsorbed water and hydroxyl groups also increased which was identified by FTIR. It has been proven carbon content in the modified paste and efficient mixing of carbon spheres and TiO_2 paste. The broad peak observable in the second step of pure TiO_2 paste (has $\Delta m = 9.85\%$) can be explained by the decomposition of the ethyl cellulose. It is possible to see that carbon burning in C-TiO_2 paste causes some alteration in the weight loss in this stage. Those occurring between 310 and 490 °C (4.23 wt% loss) also correspond to the crystallization from the amorphous phase into anatase and decrease of carbons. The TGA of modified TiO_2 paste reveals that the solvent and binder and carbon templates (totally removed mass percentage of 85.34%) burn out completely only at 530 °C.

TGA curves exhibited that decomposition temperature for both of them is rather the same because of the small amounts of carbon spheres into TiO_2 paste. The increase in thermal stability of C-TiO_2 originates as a result of interactions between homogeneously mixed carbon spheres and TiO_2 particles. This interaction undoubtedly restricts the thermal motion of TiO_2 particles which enhances the rigidity of TiO_2 layer and more energy needs for the movement of particles.

When the calcination temperature reaches 300 °C, TiO_2 nanoparticles have not been compactly connected with each other yet, the carbonaceous sphere templates start to burn and decrease in the size while retaining their spherical profiles

during calcination. In this stage, due to the expansion of gas generated by carbon spheres the hollow void spheres formed in the bigger size than the diameter of carbon spheres. So TiO_2 nanoparticles at the edges of pores are tightly packed but in the later stage ethyl cellulose will be burned out and TiO_2 nanoparticles connect to each other and size of hollow spheres become smaller. Annealing at 450 °C for 30 min, ensure excellent binding between the TiO_2 particles and the conversion of any remaining amorphous TiO_2 to anatase phase.

2.3. Deposition of Perovskite on Modified C-TiO_2 Layers

In the present study, we fabricated a compact and pin-hole free perovskite film with full coverage on the TiO_2 layer via atmospheric pressure vapor assisted solution process (AP-VASP) method.[32–34] Details of $CH_3NH_3PbI_3$ deposition using AP-VASP method can be found in Supporting Information.

Figure 6a–d shows the FESEM images and grain size distributions for $MAPbI_3$ deposited on the pure (C0) and modified TiO_2 layers with varied proportions of carbon spheres 4 wt% (C4), 8 wt% (C8), and 10 wt% (C10), respectively. As shown in Figure 6, the morphology of perovskite changes drastically on different TiO_2 layers; the average grain size of the perovskite crystals increases substantially from 525 nm for a standard cell to 750 nm for the modified cell as the carbon sphere contents increase from 0 to 8 wt%. For the perovskite film fabricated on C8 TiO_2 layer, we can clearly observe high uniformity and 100% coverage of the perovskite film. A further increase in the TiO_2 film porosity to C10 resulted in observe small and large pores inside the perovskite film which is indicative of the nonhomogeneous and incomplete coverage of the surface with perovskite films and difficulty of obtaining devices with good PCE from these layers.

The FESEM images of deposited $CH_3NH_3PbI_3$ films on both TiO_2 and C8-TiO_2 films show rather homogeneous surfaces with no indications of pinhole defects. Fine-tuning porosity
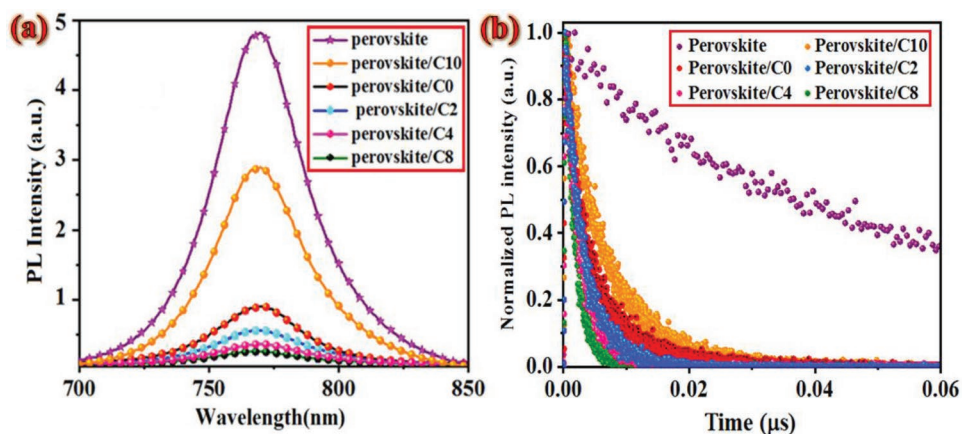
**ADVANCED
SCIENCE NEWS**
www.advancedsciencenews.com

**ADVANCED
MATERIALS
INTERFACES**
www.advmatinterfaces.de

Figure 7. a) The Photoluminescence (PL) spectra, and b) transient PL decay profiles of $CH_3NH_3PbI_3$ deposited on glass and varied C-TiO$_2$ ETLs. Transient PL decays were obtained using the TCSPC technique with excitation at 635 nm and probe at 770 nm.

optimization of C-TiO$_2$ films results in very well penetration of MAI into the pores of TiO$_2$ and creating a uniform, continuous, and homogeneous compact $CH_3NH_3PbI_3$ film with a complete surface coverage of larger grain sizes (Figure 6). Perovskite film with larger grain size causes to mitigate the possibility of trap states or carrier blocking at grain boundaries.

Steady-state photoluminescence (PL) measurements of perovskite deposited on the TiO$_2$ layers with different carbon spheres contents were performed (**Figure 7**a). The PL intensities show an order C10> C0 > C2 > C4> C8, indicating that the quenching of PL of perovskite occurred when it was deposited in the TiO$_2$ films due to electrons injecting from perovskite into these ETLs. The C8 film shows the most PL quenching compared to the other films due to its better effect of pore filling than the others that lead to the improved interconnection on the C8/$CH_3NH_3PbI_3$ interface. The corresponding bandgap (E_g = 1.61 eV) determined from the PL spectra is in good agreement with previous studies.[40,56,57]

To investigate further the charge extraction process at the perovskite/ETL interface, affecting their corresponding photovoltaic performances, we measured transient PL decay for perovskite layers deposited on glass, pure and modified TiO$_2$ films using the time correlated single photon counting (TCSPC) technique with excitation at 635 nm and probe at 770 nm. The PL transient profiles shown in Figure 7b were well fitted with a bi-exponential decay function with a fast component τ_1 and a slow component τ_2 (Figure S2, Supporting Information). The fitted time coefficients (τ_i), and the corresponding relative amplitudes (A_i) for each sample are listed in **Table 1**. The average PL lifetimes (τ_{PL}) were determined with an intensity-averaged approach according to the following equation[58]

$$\tau_{PL} = \frac{\sum A_i \tau_i^2}{\sum A_i \tau_i} \tag{1}$$

in which A_i and τ_i are the amplitudes of each component and the corresponding fitted time coefficients, respectively. Assuming that all PL quenches are due to the effect of electron extraction, the interfacial electron extraction time (τ_e) at the

interface between $CH_3NH_3PbI_3$ and mp-TiO$_2$ can be predicted using the following equation

$$\frac{1}{\tau_e} = \frac{1}{\tau_{PSK/ETL}} - \frac{1}{\tau_{PSK}} \tag{2}$$

in which τ_{PL} and $\tau_{PSK/ETL}$ are the PL lifetimes for $CH_3NH_3PbI_3$ only deposited on glass and those with $CH_3NH_3PbI_3$ deposited onto varied mp-TiO$_2$ layers, respectively. τ_{PL} was determined to be 133.68 ns but decreased to 6.79, 9.36, 12.75, 16.31, and 63.84 ns when $CH_3NH_3PbI_3$ layer was in contact with the mp-TiO$_2$ of C8, C4, C2, C0, and C10, respectively.

The electron extraction time (τ_e) in the $CH_3NH_3PbI_3$/mp-TiO$_2$ interface shows the order τ_e (C8) < τ_e (C4) < τ_e (C2) < τ_e (C10). The trend of electron extraction rate coefficients (1/τ_e) shows the order τ_e (C8) > τ_e (C4) > τ_e (C2) > τ_e (C10), indicating that C8 is the most efficient ETL compared to all ETLs. This order is consistent with the trend of their photovoltaic results reported in Figures 3 and 4, indicating the superior electron-extracting characteristic of the C8 layer as an efficient ETL responsible for the high-performance $CH_3NH_3PbI_3$ based solar cells. The C8 ETL possessed a stronger electron extraction capability than the pure and other modified ETLs, which is consistent with the trend of PL quenching in Figure 7a.

Table 1. The photoluminescence fitted time coefficients, corresponding amplitudes of each component in the bi-exponential decay function, and the interfacial electron extraction times (τ_e) at the interface of deposited $CH_3NH_3PbI_3$ on modified mp-TiO$_2$ layers fabricated on glass substrates with excitation at 635 nm and probe at 770 nm.

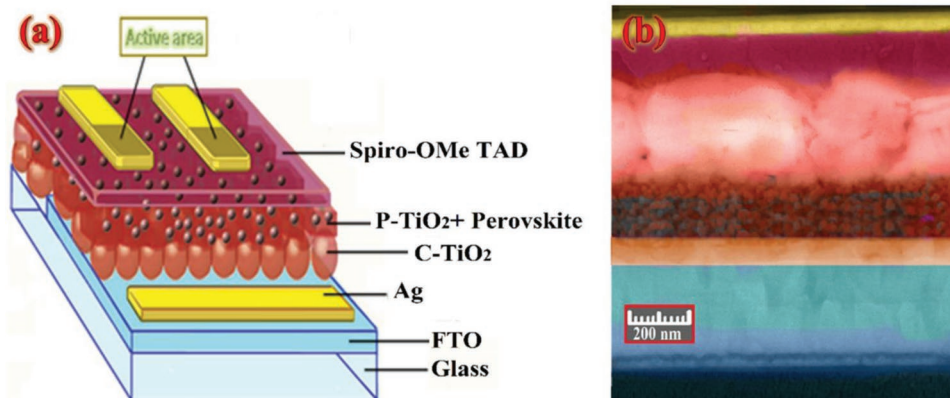|	τ_1 [ns]	A_1	τ_2 [ns]	A_2	τ_e [ns]
Perovskite	54.6	24%	143.2	76%	–
perovskite/C10	14.0	36%	48.0	64%	63.84
perovskite/C0	7.16	48%	17.35	52%	16.31
perovskite/C2	7.18	56%	14.46	44%	12.75
perovskite/C4	4.21	60%	11.29	40%	9.36
perovskite/C8	3.76	59%	8.24	41%	6.79

Figure 8. a) Schematic representation of the fabricated device structure; Spiro-OMeTAD used as a hole-transport layer (HTL) and a silver electrode is evaporated on top as a counter electrode. The active area of the cells was fixed at 9 mm² (3 mm × 3 mm) using a metal mask and b) The corresponding side-viewed FESEM image of standard solar cell with the scale bar indicating 200 nm. Size of particles and thickness of layers are not in scale.

2.4. Device Performance

The PSC devices were fabricated according to a layer-by-layer procedure detailed in the Supporting Information. **Figure 8**a,b shows the schematic representation of a fabricated device and side-view of a standard device, respectively.

As can see in **Table 2**, the obtained performance of the C8 device is much greater than that of the C0 device (PCE of 11.72%) and is also greater than that reported elsewhere for the best efficiency of a device fabricated using the AP-VASP method in ambient air condition.[33]

The higher FF of samples made of modified TiO₂ films from C2 to C8 in **Figure 9** is attributed mainly to the better infiltration of deposited perovskite on the modified TiO₂ layer, larger $CH_3NH_3PbI_3$ grains and uniform covering the entire substrate,

which improve light-harvesting properties. It shows that the modification on the surface reduces the loss of photoexcited carriers being extracted from the device due to the suppression of surface electron recombination. The increase in short circuit current density is also evidenced for better light absorption and light scattering of the optimized TiO₂ layer.

Higher charge concentration in the interface of TiO₂ and perovskite absorber for a certain number of injected electrons leads to retarding the recombination in PSC and getting high V_{oc} and PCE. In C10 samples, the big voids in mesoporous TiO₂ films would cause direct contact between the electron transporting layer and hole transporting layer, leading to poor device performance. Thus, the addition of further carbon spheres causes the efficiency of C10 to be lower than that of the standard device.

The extent of discrepancy between the J_{sc} obtained from the J–V curve and the J_{sc} calculated based on IPCE data, in Figure 9f, might be due to differences in the morphology of deposited $CH_3NH_3PbI_3$ layer on different ETLs and/or discrepancy in interfacial contacts.

Enlarging the interfacial contact between perovskite and TiO₂ by effective pore-filling suppresses the charge accumulation caused by ion migration and diminishes the possibility of hysteresis. The J–V characteristics of the $CH_3NH_3PbI_3$ based solar cells prepared with varying porosity of TiO₂ film in forward and reverse scans are shown in **Figure 10**. Obviously, the hysteresis effects have been significantly relieved compared with the standard devices without porosity modification of ETL. The hysteresis behavior in the J–V characteristics of perovskite solar cells substantially reduced due to good pore filling, large $CH_3NH_3PbI_3$ crystal, and better ion migration in the presence of modified TiO₂ layer.

In order to describe the hysteresis behavior of devices, a J–V hysteresis index (HI) has been introduced to numerically estimate the difference of current densities between forward and reverse sweep scan of devices.[59–61] The observed hysteresis can be quantified by calculating the HI as follows

Table 2. Photovoltaic parameters of perovskite solar cells fabricated with varied porosity of mesoporous TiO₂ layer measured under simulated AM-1.5G illumination with active area of 0.09 cm².

[a]ETL		J_{SC} [mA cm⁻²]	V_{OC} [V]	FF [%]	PCE [%]
C0	[b]Average	17.96 ± 0.24	0.98 ± 0.00	60.59 ± 0.29	10.73 ± 0.11
	[c]Best	20.15	0.973	59.77	11.72
C2	[b]Average	18.91 ± 0.30	0.99 ± 0.00	64.35 ± 0.67	12.11 ± 0.15
	[c]Best	21.73	0.979	61.4	13.06
C4	[b]Average	20.55 ± 0.30	1.00 ± 0.00	65.06 ± 0.67	13.34 ± 0.15
	[c]Best	22.19	1.024	65.49	14.90
C8	[b]Average	21.82 ± 0.23	1.02 ± 0.00	69.68 ± 0.71	15.60 ± 0.12
	[c]Best	23.66	1.046	67.33	16.66
C10	[b]Average	14.39 ± 0.25	0.86 ± 0.00	61.12 ± 0.45	7.58 ± 0.13
	[c]Best	14.79	0.95	59.61	8.35

[a]The devices were fabricated using the $CH_3NH_3PbI_3$ layers prepared via a two-step AP-VASP method onto the different electron-transporting layers (ETLs) detailed in the Experimental Methods, Supporting Information; [b]The average values shown in parentheses with the uncertainties representing one standard deviation were obtained from 25 devices fabricated under the same experimental conditions; [c]The best photovoltaic performances are reported for each type of C-modified devices.

$$\text{hysteresis index} = \frac{J_{RC}(0.8V_{oc}) - J_{FD}(0.8V_{oc})}{J_{RC}(0.8V_{oc})} \qquad (3)$$

**ADVANCED
SCIENCE NEWS**
www.advancedsciencenews.com

**ADVANCED
MATERIALS
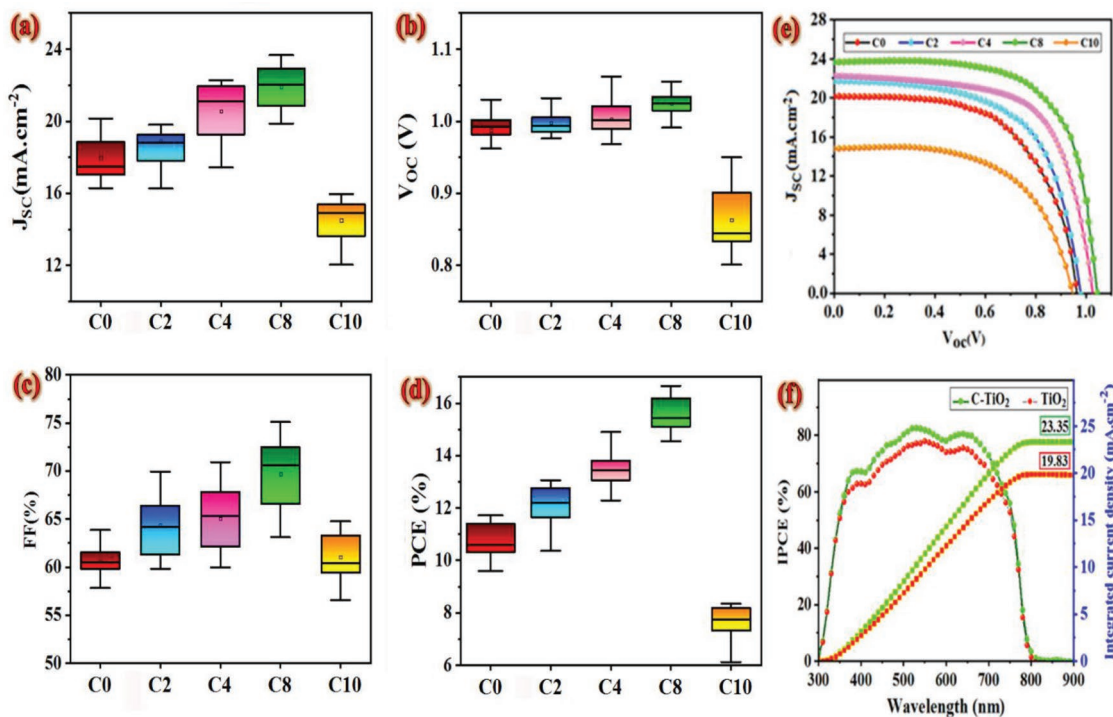INTERFACES**
www.advmatinterfaces.de

Figure 9. Boxplots of photovoltaic parameters a) J_{SC}, b) V_{OC}, c) FF, and d) PCE for devices made of C0, C2, C4, C8, and C10 TiO_2 paste as ETLs. Each data set is carried out from at least 25 devices. e) Current density–voltage curves of best efficiency devices and f) IPCE and integrated current density of the best device in comparison with standard device.

where J_{RS} (0.8 V_{oc}) and J_{FD} (0.8 V_{oc}) represent the current density at 80% of V_{oc} voltage value for the reverse (from V_{oc} to zero) and forward (from zero to V_{oc}) voltage scans, respectively. The value of the HI presents the extent of hysteresis, a HI value of zero reflects a device without hysteresis while higher values of HI indicate a more pronounced hysteresis. The solar cell parameters values, along with the calculated hysteresis index of standard and modified devices are summarized in **Table 3** depending on the scan direction.

It has been already suggested in the previous literatures that the origin of observed hysteresis could be related to the grain size of the perovskite layer.[59–61] The increase of average grains size leads to fewer grain boundaries in the perovskite layer and improves the measurable PCEs by increasing the perovskite layer smoothness and rate of electron transfer from the perovskite layer to the mp-TiO_2. According to the HI calculations, small perovskite grains size of 525 nm shows a high hysteresis index of 0.153 compared with 0.060 for larger grains size of 750 nm in perovskite layer of the modified device. The calculations numerically confirm that the porosity modification of TiO_2 layer onto the hysteresis reduction prevents charge carriers from easily trapping or recombination at the grain boundaries and perovskite interfaces due to the low defect density.[61–66]
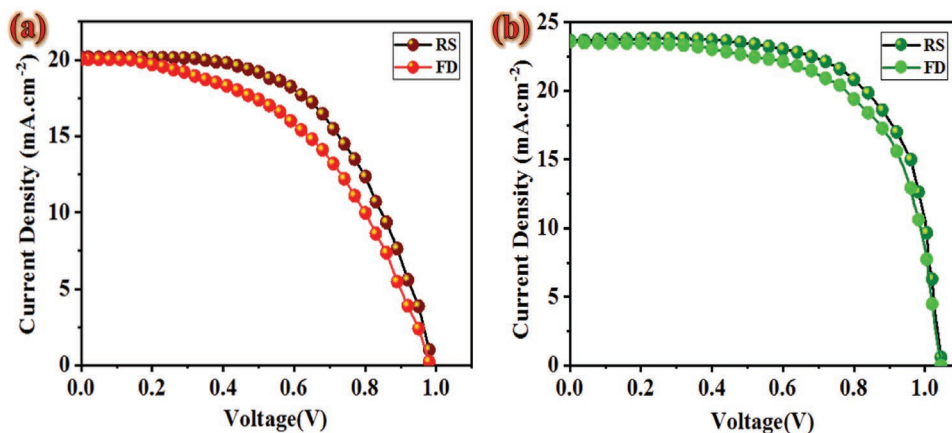

Figure 10. J–V characteristics of the devices based on devices in contact to a) TiO_2 and b) C-TiO_2 layers, under illumination condition in reverse and forward sweep directions. These devices were measured under simulated AM1.5 and 100 mW cm^{-2} sun light.

Table 3. Photovoltaic parameters at forward (FD) and reverse (RS) sweep scan direction obtained using a rate of 100 mV s^{-1} starting from forward bias. The cells were masked with a black metal mask with a limit active area of 0.09 cm^2 and the hysteresis index was calculated by Equation (3).

$CH_3NH_3PbI_3$ size [nm]	Scan direction	J_{sc} [mA cm^{-2}]	V_{oc} [V]	FF	PCE [%]	HI
525	FD	20.06	0.96	49.86	9.6	0.153
	RS	20.16	0.973	59.75	11.72	
750	FD	23.58	1.04	62.34	15.29	0.060
	RS	23.67	1.045	67.33	16.66	

The long-term stability of unencapsulated PSCs has been investigated during a period of 30 days, at a relative humidity of 33%. Daily measurement of J–V characteristic is carried out on the best-performing devices, which is kept in darkness in ambient air in the intervals between measurements. **Figure 11** shows the related photovoltaic parameters of the preliminary stability investigation during 30 days. The modified solar cells sustained over 91% of the initial PCE, while the pristine perovskite solar cells showed 39% decrease in its initial PCE.

3. Conclusions

We have studied the effect of porosity modification of the TiO$_2$ layer with different contents of carbon spheres on the grain size of perovskite layers under relatively high humidity

ambient conditions (≥50%), the performance and stability of CH$_3$NH$_3$PbI$_3$ solar cells. The CH$_3$NH$_3$PbI$_3$ films were deposited via a highly reproducible AP-VASP method. Up to date, the best reported efficiency for the fabrication of CH$_3$NH$_3$PbI$_3$ based PSCs by AP-VASP method has only reached to the 13.5%.[33] In the present study, modification of ETL porosity resulted in the feasible incorporation of MAI to the modified porous TiO$_2$ films and producing larger crystal grains of perovskite in ambient air with relatively high humidity. The efficiency of the PSC device with 8 wt% carbon spheres has been further improved to 16.66%, which is significantly greater than the device without C-modification (PCE 11.72%). The SEM images showed compact perovskite films with the grain size up to micrometers in the modified CH$_3$NH$_3$PbI$_3$-TiO$_2$ heterojunction film whereas the pristine CH$_3$NH$_3$PbI$_3$-TiO$_2$ film exhibited smaller grains size. The improvement in the quality of perovskite film results in more contact between the C-TiO$_2$ layer and the CH$_3$NH$_3$PbI$_3$ active layer, better electron injection and less hysteresis of the device. The interface engineering by porosity modification of TiO$_2$ film would increase the electron-injection rate and suppress the charge recombination at the CH$_3$NH$_3$PbI$_3$-TiO$_2$ interface, which could significantly reduce the resistance for electrons to transfer to the FTO surface, improve the stability of fabricated PSCs in ambient air, and pave the way to their further commercialization. The fact that there is a more gradually large decrease in the efficiency of standard devices than the modified devices in the same conditions provides direct evidence of the beneficial effect of porosity modification on PSC photostability.
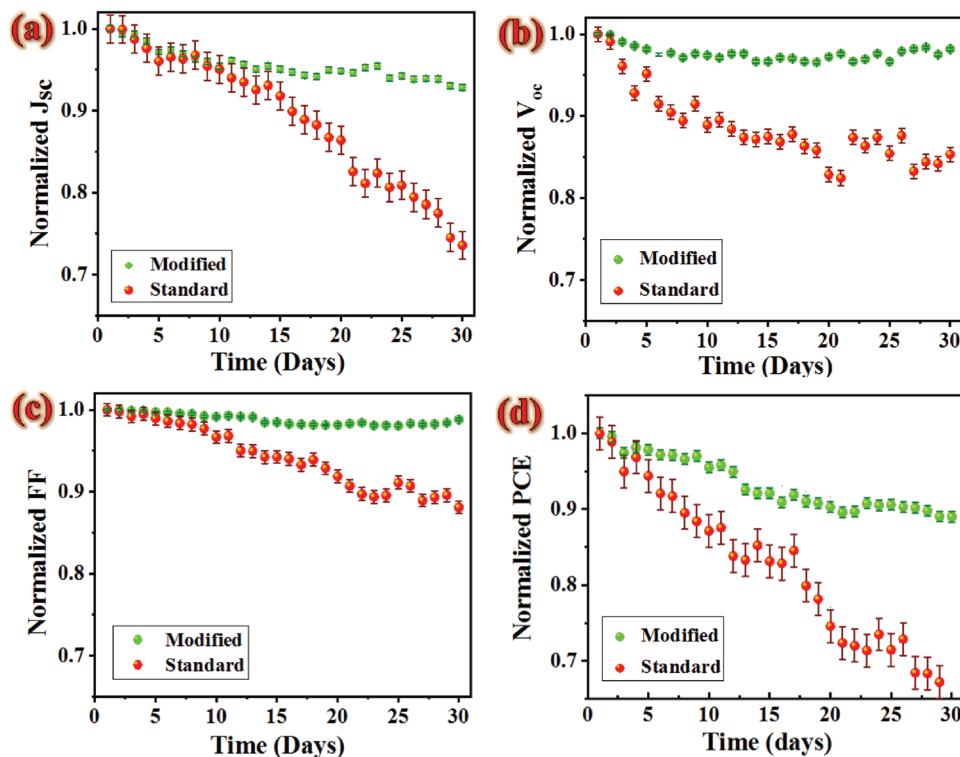

Figure 11. Normalized photovoltaic parameters of standard, and modified CH$_3$NH$_3$PbI$_3$ based PSCs measured during 30 days under ambient room condition (25–30 °C, 33% humidity). Solar cell characterization of nonencapsulated best-performing modified devices indicates 91% maintenance of its PCE after 30 days.

Conflict of Interest

The authors declare no conflict of interest.

[1] National Renewable Energy Laboratory (NREL) Best research-cell efficiency chart, https://www.nrel.gov/pv/assets/pdfs/best-research-cell-efficiencies.20190802.pdf (accessed: November 2019).

[2] Y. Cheng, X. Xu, Y.-M. Xie, H.-W. Li, J. Qing, C. Ma, C.-S. Lee, F. So, S.s-W. Tsang, *Sol. RRL* **2017**, *1*, 1770131.

[3] C. Zuo, D. Vak, D. Angmo, L. Ding, M. Gao, *Nano Energy* **2018**, *46*, 185.

[4] Y. Cheng, F. So, S.-W. Tsang, *Mater. Horiz.* **2019**, *6*, 1611.

[5] F. Li, C. Wang, P. Liu, Y. Xiao, L. Bai, F. Qi, X. Hou, H. Zhang, Y. Wang, S. Wang, X.-Z. Zhao, *Sol. RRL* **2018**, *3*, 1800297.

[6] A. K. Baranwal, H. Kanda, N. Shibayama, S. Ito, *Sustainable Energy Fuels* **2018**, *2*, 2778.

[7] A. D. Maria, V. L. Ferrara, G. Rametta, L. V. Mercaldo, A. Bruno, F. Matteocci, A. D. Carlo, P. D. Veneri, *20th Italian National Conf. on Photonic Technologies (Fotonica 2018)*, Lecce, Italy **2018**.

[8] H. Zhou, Q. Chen, G. Li, S. Luo, T.-B. Song, H.-S. Duan, Z. Hong, J. You, Y. Liu, Y. Yang, *Science* **2014**, *345*, 542.

[9] G. Xing, N. Mathews, S. Sun, S. S. Lim, Y. M. Lam, M. Gratzel, S. Mhaisalkar, T. C. Sum, *Science* **2013**, *342*, 344.

[10] T.-B. Song, Q. Chen, H. Zhou, C. Jiang, H.-H. Wang, Y. Yang, Y. Liu, J. You, Y. Yang, *J. Mater. Chem. A* **2015**, *3*, 9032.

[11] Z. Yao, W. Wang, H. Shen, Y. Zhang, Q. Luo, X. Yin, X. Dai, J. Li, H. Lin, *Sci. Technol. Adv. Mater.* **2017**, *18*, 253.

[12] S. M. Seyed-Talebi, M. Neek-Amal, *J. Appl. Phys.* **2014**, *116*, 153507.

[13] S. M. Seyed-Talebi, J. Beheshtian, *Phys. B* **2013**, *429*, 52.

[14] S. M. Seyed-Talebi, I. Kazeminezhad, J. Beheshtian, *Phys. Chem. Chem. Phys.* **2015**, *17*, 29689.

[15] L. L. Zhang, X. S. Zhao, *Chem. Soc. Rev.* **2009**, *38*, 2520.

[16] A. A. Mamun, T. T. Ava, K. Zhang, H. Baumgart, G. Namkoong, *Phys. Chem. Chem. Phys.* **2017**, *19*, 17960.

[17] C. Liu, M. Cai, Y. Yang, Z. Arain, Y. Ding, X. Shi, P. Shi, S. Ma, T. Hayat, A. Alsaedi, J. Wu, S. Dai, G. Cao, *J. Mater. Chem. A* **2019**, *7*, 11086.

[18] W. Zhou, F. Sun, K. Pan, G. Tian, B. Jiang, Z. Ren, C. Tian, H. Fu, *Adv. Funct. Mater.* **2011**, *21*, 1922.

[19] J. H. Pan, X. S. Zhao, W. I. Lee, *Chem. Eng. J.* **2011**, *170*, 363.

[20] A. Rapsomanikis, D. Karageorgopoulos, P. Lianos, E. Stathatos, *Sol. Energy Mater. Sol. Cells* **2016**, *151*, 36.

[21] C.-C. Chung, C. S. Lee, E. Jokar, J. H. Kim, E. W.-G. Diau, *J. Phys. Chem. C* **2016**, *120*, 9619.

[22] J. Shao, S. Yang, L. Lei, Q. Cao, Y. Yu, Y. Liu, *Chem. Mater.* **2016**, *28*, 7134.

[23] S. Hore, C. Vetter, R. Kern, H. Smit, A. Hinsch, *Sol. Energy Mater. Sol. Cells* **2006**, *90*, 1176.

[24] W. Ke, G. Fang, J. Wang, P. Qin, H. Tao, H. Lei, Q. Liu, X. Dai, X. Zhao, *ACS Appl. Mater. Interfaces* **2014**, *6*, 15959.

[25] M. Singh, C.-H. Chiang, K. M. Boopathi, C. Hanmandlu, G. Li, C.-G. Wu, H.-C. Lin, C.-W. Chu, *J. Mater. Chem. A* **2018**, *6*, 7114.

[26] S. L W. A. Daoud, *J. Mater. Chem. A* **2015**, *3*, 8992.

[27] H. Wang, R. Jiang, M. Sun, X. Yin, Y. Guo, M. He, L. Wang, *J. Mater. Chem. C* **2019**, *7*, 1948.

[28] K. Mahmood, S. Sarwarb, M. T. Mehran, *RSC Adv.* **2017**, *7*, 17044.

[29] G. Yang, J. Zhang, P. Wang, Q. Sun, J. Zheng, Y. Zhu, *Curr. Appl. Phys.* **2011**, *11*, 376.

[30] M. Marandi, S. Feshki, M. Naeimi Sani Sabet, Z. Anajafi, N. Taghavinia, *RSC Adv.* **2014**, *4*, 58064.

[31] Q. Zhang, D. Myers, J. Lan, S. A. Jenekhe, G. Cao, *Phys. Chem. Chem. Phys.* **2012**, *14*, 14982.

[32] R. Sedighi, F. Tajabadi, S. Shahbazi, S. Gholipour, N. Taghavinia, *ChemPhysChem* **2016**, *17*, 2382.

[33] R. Sedighi, F. Tajabadi, N. Taghavinia, *Electrochim. Acta* **2018**, *259*, 485.

[34] H. Pourradi, K. Ghani, M. Mahdavi, *J. Phys. Chem. C* **2019**, *123*, 4044.

[35] T. Du, C. H. Burges, J. Kim, J. Zhang, J. R. Durrant, M. A. McLachlan, *Sustainable Energy Fuels* **2017**, *1*, 119.

[36] X. Sun, J. Xu, L. Xiao, J. Chen, B. Zhang, J. Yao, S. Dai, *Int. J. Photoenergy* **2017**, *2017*, 4935265.

[37] H. Chen, Z. Wei, H. He, X. Zheng, K. S. Wong, S. Yang, *Adv. Energy Mater.* **2016**, *6*, 1502087.

[38] B.-E. Cohen, L. Etgar, *Front. Optoelectron.* **2016**, *9*, 44.

[39] Y. Li, B. Ding, G.-J. Yang, C.-J. Li, C.-X. Li, *J. Mater. Sci. Technol.* **2018**, *34*, 1405.

[40] Q. Chen, H. Zhou, T.-B. Song, S. Luo, Z. Hong, H.-S. Duan, L. Dou, Y. Liu, Y. Yang, *Nano Lett.* **2014**, *14*, 4158.

[41] H. K. Adli, T. Harada, W. Septina, S. Hozan, S. Ito, S. Ikeda, *J. Phys. Chem. C* **2015**, *119*, 22304.

[42] J. Jiang, H. J. Tao, S. Chen, B. Tan, N. Zhou, L. Zhu, Y. Zhao, Y. Wang, J. Tao, *Appl. Surf. Sci.* **2016**, *371*, 289.

[43] S. Wang, W. Dong, X. Fang, Q. Zhang, S. Zhou, Z. Deng, R. Tao, J. Shao, R. Xia, C. Song, L. Hu, J. Zhu, *Nanoscale* **2016**, *8*, 6600.

[44] M. Jung, S.-G. Ji, G. Kim, S. I. Seok, *Chem. Soc. Rev.* **2019**, *48*, 2011.

[45] Y. H. Lee, J. Luo, R. Humphry-Baker, P. Gao, M. Gratzel, M. K. Nazeeruddin, *Adv. Funct. Mater.* **2015**, *25*, 3925.

[46] Z. Y. Wu, B.-L. Jian, H.-C. Hsu, *Opt. Mater. Express* **2019**, *9*, 1882.

[47] H. Wei, Y. Tang, B. Feng, H. You, *Chin. Phys. B* **2017**, *26*, 128801.

[48] S.-Y. Kim, H. J. Jo, S.-J. Sung, D.-H. Kim, *APL Mater.* **2016**, *4*, 100901.

[49] C. Liu, J. Fan, X. Zhang, Y. Shen, L. Yang, Y. Mai, *ACS Appl. Mater. Interfaces* **2015**, *7*, 9066.

[50] Q. Chen, H. Zhou, Z. Hong, S. Luo, H.-S. Duan, S.-H. Wang, Y. Liu, G. Li, Y. Yang, *J. Am. Chem. Soc.* **2014**, *136*, 622.

[51] S. Chen, L. Lei, S. Yang, Y. Liu, Z.-S. Wang, *ACS Appl. Mater. Interfaces* **2015**, *7*, 25770.

[52] S. M. Seyed-Talebi, I. Kazeminezhad, M. Nematpour, *J. Catal.* **2018**, *361*, 339.

[53] S. M. Seyed-Talebi, I. Kazeminezhad, H. Motamedi, *Ceram. Int.* **2018**, *44*, 13457.

[54] V. G. Pol, M. Motiei, A. Gedanken, J. Calderon-Moreno, M. Yoshimura, *Carbon* **2004**, *42*, 111.

[55] S. Ito, T. N. Murakami, P. Comte, P. Liska, C. Grätzel, M. K. Nazeeruddin, M. Grätzel, *Thin Solid Films* **2008**, *516*, 4613.

[56] M. Saba, M. Cadelano, D. Marongiu, F. Chen, V. Sarritzu, N. Sestu, C. Figus, M. Aresti, R. Piras, A. G. Lehmann, C. Cannas, A. Musinu, F. Quochi, A. Mura, G. Bongiovann, *Nat. Commun.* **2014**, *5*, 5049.

[57] C. M. Sutter-Fella, Y. Li, N. Cefarin, A. Buckley, Q. P. Ngo, A. Javey, I. D. Sharp, F. M. Toma, *J. Visualized Exp.* **2017**, *127*, e55404.

[58] A. E. Shalan, T. Oshikiri, S. Narra, M. M. Elshanawany, K. Ueno, H.-P. Wu, K. Nakamura, X. Shi, E. W.-G. Diau, H. Misawa, *ACS Appl. Mater. Interfaces* **2016**, *8*, 33592.

[59] T. P. Gujar, T. Unger, A. Schönleber, M. Fried, F. Panzer, S. V. Smaalen, A. Köhler, M. Thelakkat, *Phys. Chem. Chem. Phys.* **2018**, *20*, 605.

[60] N. Tripathi, M. Yanagida, Y. Shirai, T. Masuda, L. Han, K. Miyano, *J. Phys. Chem. A* **2015**, *3*, 12088.

[61] H.-S. Kim, N.-G. Park, *J. Phys. Chem. Lett.* **2014**, *5*, 2927.

[62] H. Li, G. Wu, W. Li, Y. Zhang, Z. Liu, D. Wang, S. Liu, *Adv. Sci.* **2019**, *6*, 1901241.

[63] J. Wei, Y. Zhao, H. Li, G. Li, J. Pan, D. Xu, Q. Zhao, D. Yu, *J. Phys. Chem. Lett.* **2014**, *5*, 3937.

[64] Y. Shao, Y. Fang, T. Li, Q. Wang, Q. Dong, Y. Deng, Y. Yuan, H. Wei, M. Wang, A. Gruverman, J. Shield, J. Huang, *Energy Environ. Sci.* **2016**, *9*, 1752.

[65] X. Cao, Y. Li, C. Li, F. Fang, Y. Yao, X. Cui, J. Wei, *J. Phys. Chem. C* **2016**, *120*, 22784.

[66] L. Wang, C. McCleese, A. Kovalsky, Y. Zhao, C. Burda, *J. Am. Chem. Soc.* **2014**, *136*, 12205.